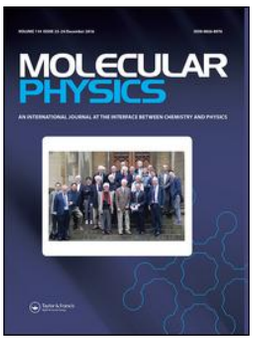

Taylor & Francis
Taylor & Francis Group

Molecular Physics

An International Journal at the Interface Between Chemistry and Physics

ISSN: 0026-8976 (Print) 1362-3028 (Online) Journal homepage: https://www.tandfonline.com/loi/tmph20

Comparative assessment of the ELBA coarse-grained model for water

Mario Orsi

To cite this article: Mario Orsi (2014) Comparative assessment of the ELBA coarse-grained model for water, Molecular Physics, 112:11, 1566-1576, DOI: 10.1080/00268976.2013.844373

To link to this article: https://doi.org/10.1080/00268976.2013.844373

Molecular Physics, 2014
Vol. 112, No. 11, 1566–1576, http://dx.doi.org/10.1080/00268976.2013.844373

Taylor & Francis
Taylor & Francis Group

RESEARCH ARTICLE

Comparative assessment of the ELBA coarse-grained model for water

Mario Orsi*

School of Engineering and Materials Science, Queen Mary University of London, London, UK

(*Received 2 August 2013; accepted 6 September 2013*)

The ELBA force field for water consists of a single spherical site embedded with a point dipole. This coarse-grained model is assessed here through the calculation of fundamental properties of bulk liquid water and the water–vapour interface. Accuracy and efficiency are evaluated and compared against simulations of standard three- and four-site atomistic models. For bulk liquid systems, ELBA reproduces accurately most of the investigated properties. However, the radial distribution function deviates from atomistic and experimental data, indicating a loss of local structure. The water–vapour interface, simulated over a range of temperatures from 300 to 600 K, is captured realistically in terms of its density distribution, and the accuracy in reproducing the experimental surface tension is as high as that of the best atomistic model. The critical temperature of ELBA is also found to be in excellent agreement with experiment. However, the interfacial electric field and surface potential are missing. The computational speed-up of ELBA compared to traditional atomistic models is estimated to be between one and two orders of magnitude.

Keywords: water; molecular dynamics; coarse-grained; surface tension; surface potential

1. Introduction

Owing to its ubiquity and importance in numerous areas of science and technology, water is probably the most studied material in the scholarly literature [1,2]. In particular, the investigation of water by computer simulation has been a very active research area for about four decades now; multitudes of models have been developed, at many levels of abstraction [3–11].

In this work, we consider the coarse-grained ELBA model for water, originally developed as a solvent for lipid membranes [12,13], and we investigate its ability to reproduce fundamental properties of bulk liquid water and the water–vapour interface. In general, coarse-grained modelling involves using single particles to represent collections of nearby atoms, with the aim of reducing the computational cost while retaining fundamental physical features [14–16]. In the ELBA force field, the three atoms of a water molecule are represented with one site, which consists of a point dipole affixed to the centre of a Lennard-Jones sphere.

Results from ELBA will be compared to experimental data from the literature and simulation data obtained here for standard empirical non-polarisable rigid models [17–21]. In all the calculations, we employ larger system sizes and longer simulation times than typically reported, to obtain highly precise predictions and facilitate comparison. Long simulation times (ideally combined with large system sizes) are especially important when studying the water–vapour interface close to room temperature, because of the very slow evaporation rate and slow convergence of the calculation of key properties (such as the surface tension). Full details of models and methods are given in Section 2.

Results are reported and discussed in Section 3. Liquid bulk systems are investigated with respect to their basic physical properties, including density, potential energy, heat of vaporisation, diffusion, and local structure (through the radial distribution function). Regarding the liquid–vapour interface, we evaluate density profiles and compute the surface tension for a range of temperatures. Moreover, we analyse electrical features in terms of electrostatic potential profiles and corresponding electric fields. In Section 4, ELBA is further compared to alternative coarse-grained models, using data available in the literature. Finally, the main findings of our study are summarised in Section 5.

2. Models and methods

2.1. ELBA coarse-grained force field

In the ELBA model [12,13], a water molecule is described by a single interaction site, comprising a Lennard-Jones sphere embedded with a point dipole. The total potential energy U_{ij} of an interacting pair of sites i, j is

$$U_{ij} = U_{ij}^{\mathrm{LJ}} + U_{ij}^{\mathrm{dip}}, \tag{1}$$

*Email: m.orsi@qmul.ac.uk

with U_{ij}^{LJ} representing the Lennard-Jones term and U_{ij}^{dip} the point dipole term. The general 'Lennard-Jones plus point dipole' model, also known as the Stockmayer model, is mainly used to study ideal polar particles, in reduced units [22–27]. The ELBA force field is a novel parametrisation of the Stockmayer potential aimed at modelling a real material (water), in physical units [28,29]. ELBA is also unique in that both the terms of Equation (1) are actually 'shifted-force' variants of the corresponding original potentials. In general, shifted-force schemes involve altering the form of an intermolecular potential so that both the potential energy and its derivative go to zero smoothly at the cut-off [30,31]. This improves energy conservation (thus permitting longer integration timesteps) and removes cut-off-related artifacts in the particles' motion, which are especially problematic for orientation-dependent potentials, such as the point dipole potential [32]. For the Lennard-Jones term, we use the following expression proposed by Stoddard and Ford [33]:

$$U_{ij}^{\mathrm{LJ}} = 4\epsilon\left\{\left[\left(\frac{\sigma}{r}\right)^{12} - \left(\frac{\sigma}{r}\right)^{6}\right] + \left[6\left(\frac{\sigma}{r_c}\right)^{12} - 3\left(\frac{\sigma}{r_c}\right)^{6}\right] \times \left(\frac{r}{r_c}\right)^{2} - 7\left(\frac{\sigma}{r_c}\right)^{12} + 4\left(\frac{\sigma}{r_c}\right)^{6}\right\}, \quad (2)$$

where r is the interparticle distance, r_c is the cut-off radius, and σ and ϵ have the standard meaning [30,31]. Regarding the dipolar component of Equation (1), we have altered the classical electrostatic model [30,34] to obtain the following original shifted-force version:

$$U_{ij}^{\mathrm{dip}} = \frac{1}{4\pi\varepsilon_0}\left[1 - 4\left(\frac{r}{r_c}\right)^{3} + 3\left(\frac{r}{r_c}\right)^{4}\right] \times \left[\frac{1}{r^3}(\boldsymbol{\mu}_i \cdot \boldsymbol{\mu}_j) - \frac{3}{r^5}(\boldsymbol{\mu}_i \cdot \boldsymbol{r})(\boldsymbol{\mu}_j \cdot \boldsymbol{r})\right], \quad (3)$$

Table 1. Parameters of the ELBA coarse-grained force field for water.

ϵ (kcal mol^{-1})	0.55
σ (Å)	3.05
μ (D)	2.6
r_c (Å)	12.0

Note: The symbols ϵ and σ stand for the conventional Lennard-Jones constants (see Equation (2)). The symbol μ denotes the magnitude of the point dipole; referring to Equation (3), $\mu = |\mu_j| = |\mu_j|$. The cut-off distance for both Lennard-Jones and point dipole interactions is r_c (see Equations (2) and (3)). In reduced units [30,32], $\epsilon^* = 1$, $\sigma^* = 1$, $\mu^* = 2.497$, and $r_c^* = 3.934$.

where ε_0 is the vacuum permittivity, $\boldsymbol{\mu}_i$ and $\boldsymbol{\mu}_j$ are the interacting point dipole vectors, $\boldsymbol{r}$ and r are, respectively, the pair distance vector and its magnitude, and r_c is the cut-off distance. Analytical expressions for the forces and torques derived from the shifted-force potentials of Equations (2) and (3) are reported in the supplementary material. The complete set of ELBA parameters can be found in Table 1.

2.2. *Atomistic force fields*

The following widely used three- and four-site water models were simulated: SPC [17], SPC/E [18], TIP3P-Ew [19,35], TIP4P-Ew [20], and TIP4P/2005 [21]. In all the atomistic simulations, a single cut-off r_c is used for both the Lennard-Jones and the real-space part of the Coulomb interactions. For SPC, SPC/E, and TIP4P-Ew, we set $r_c = 10$ Å, consistent with previous investigations [35–40]. The setting $r_c = 13$ Å was used for TIP3P-Ew [19] and TIP4P/2005 [41–43], as in the corresponding references. The complete sets of parameters used in this work to simulate atomistic water models are collected in Table 2.

2.3. *Simulation details*

Molecular dynamics simulations were run with the program LAMMPS [46]. Complete command scripts and input files are available on the author's website [47].

Table 2. Parameters of the atomistic water force fields.

	SPC	SPC/E	TIP3P-Ew	TIP4P-Ew	TIP4P/2005
ϵ_{OO}/(kcal mol^{-1})	0.15535	0.15535	0.102	0.16275	0.1852
σ_{OO}/Å	3.166	3.166	3.188	3.16435	3.1589
q_{H}/e	0.41	0.4238	0.415	0.52422	0.5564
q_{O}/e	−0.82	−0.8476	−0.83		
q_{M}/e				−1.04844	−1.1128
l_{OH}/Å	1.0	1.0	0.9572	0.9572	0.9572
l_{OM}/Å				0.125	0.1546
θ_{HOH}	109.47°	109.47°	104.52°	104.52°	104.52°
r_c/Å	10.0	10.0	13.0	10.0	13.0

Note: Subscripts H and O denote hydrogen and oxygen, respectively, while M is the additional massless site of TIP4P [20,44]. The symbols ϵ and σ are the conventional parameters of the Lennard-Jones potential [31]; note that, for all models, $\epsilon_{\mathrm{HH}} = \epsilon_{\mathrm{OH}} = \sigma_{\mathrm{HH}} = \sigma_{\mathrm{OH}} = 0$. Charges are denoted as q. The OH and OM bond lengths are represented by l_{OH} and l_{OM}, respectively. The HOH angle is represented by θ_{HOH}. The cut-off distance for both Lennard-Jones and real-space Coulomb interactions is r_c. Long-range Coulomb interactions are included for all models using the particle-particle particle-mesh (PPPM) solver [45]. Note that 'TIP3P-Ew' corresponds to the model called 'TIP3P-PME' in the original paper [19].

In the coarse-grained simulations of the ELBA model, the timestep was 10 fs; we checked the adequacy of this setting through energy conservation tests that can be found in the supplementary material. The temperature was controlled using a Langevin thermostat [48] with a collision frequency of 1 ps^{-1}. No long-range interactions were included. In the atomistic simulations, the integration timestep was 2 fs. Bonds and angles were constrained using the SHAKE algorithm [49] with a relative tolerance of 10^{-4}. Long-range Coulomb interactions were included using the particle–particle particle–mesh (PPPM) solver [45] with a relative tolerance of 10^{-5}. The temperature was controlled using a Nosé-Hoover thermostat [50] with a damping time of 0.2 ps. In all runs, the net mass centre velocity of the entire system was removed at every step. Cut-off radii were chosen as reported in Section 2.2.

Two sets of simulations were run, corresponding to two different systems: a 'bulk liquid' set and a 'liquid–vapour' set. The bulk liquid simulations were conducted at constant isotropic pressure. In the coarse-grained simulations, the pressure was controlled using the barostat by Berendsen *et al.* [51] with a damping time of 1 ps and an isothermal compressibility of 4.6×10^{-5} atm^{-1}. In the atomistic runs, we used a Parrinello-Rahman barostat [50] with a damping time of 2 ps. The liquid–vapour simulations were run at constant volume. The remaining details for each of the 'bulk liquid' and 'liquid–vapour' simulation sets are given in the following paragraphs.

2.3.1. *Bulk liquid systems*

For each of the models considered, four independent bulk liquid simulations were prepared. Each system consisted of a 6.2 nm × 6.2 nm × 6.2 nm cubic region containing 8000 water particles, corresponding to an initial density of ≈1 g cm^{-3} (consistent with that of real liquid water at room temperature). To make the four simulations for each model statistically independent from each other, initial velocities were assigned using four different random seeds. Temperature and pressure were maintained at 298 K and 1 atm, respectively (see Section 2.3 for thermostat and barostat details).

Apart from TIP3P-Ew, all the other atomistic models were simulated by including long-range corrections to the dispersion (Lennard-Jones) interactions, as is the standard practice for simulations of bulk systems [20,35,43,52,53]. We did not apply such corrections to TIP3P-Ew consistently with their absence in the original reference [19]. As for the ELBA model, the shifted-force potential (Equation (2)) is natively zero beyond the cut-off radius, and hence no corrections are needed.

Each system was simulated for 7 ns; the initial 2 ns were treated as equilibration, with the following 5 ns treated as production and used to collect data on the properties of interest.

2.3.2. *Liquid–vapour interfacial systems*

For each of the models considered, we prepared four independent systems, each initially consisting of a 6.2 nm × 6.2 nm × 6.2 nm cubic region containing 8000 water particles (density of ≈1 g cm^{-3}), as done for the bulk simulations. To obtain interfacial systems, the z dimensions of the simulation regions were extended to 24.8 nm, effectively creating vacuum to separate slabs of water parallel to the xy-plane. The volume and shape of such 6.2 nm × 6.2 nm × 24.8 nm regions were fixed throughout the simulations. To make the four runs for each model statistically independent from each other, initial velocities were assigned using four different random seeds (as done for the bulk simulations). The temperature was maintained at 300 K (see Section 2.3 for thermostat details).

Each system was simulated for 22 ns; the initial 2 ns were treated as equilibration, with the following 20 ns treated as production and used to collect data on the properties of interest.

To investigate the temperature dependence of liquid–vapour phase equilibria and surface tension for the ELBA model, additional simulations were run at temperatures of 350, 400, 450, 500, 550 and 600 K, with all other settings consistent with the above details.

2.4. *Evaluation of properties of interest*

In each simulation, properties of interest were computed during the production phase by averaging over individual values sampled every 0.2 ps. For each system simulated, four independent replicas were run (as described above); for each property of interest, four independent time averages were thus used to estimate the final means and standard errors. The numerical results (Section 3) will include a number in parentheses giving the uncertainty (as standard error) in the least significant digit; for example, 1.23(4) is to be interpreted as 1.23 ± 0.04. The bulk liquid properties (density, potential energy, heat of vaporisation, diffusion, radial distribution function) were obtained using standard procedures [4,31]. The following subsections report specific details for the somewhat more elaborate calculations of interfacial properties.

2.4.1. *Surface tension*

The liquid–vapour systems were simulated with the interfaces arranged parallel to the xy-plane of a Cartesian frame of reference. The surface tension γ_P can thus be obtained as [54,55]

$$\gamma_P = \frac{L_z}{2}\left(P_{zz} - \frac{P_{xx} + P_{yy}}{2}\right), \tag{4}$$

with L_z as the length of the simulation region along the z dimension, and P_{xx}, P_{yy}, and P_{zz} as the diagonal elements of the pressure tensor.

It is conventional (though not uncontroversial [42,56]) to supplement γ_P with the contribution to the surface tension from the interactions due to the 'tail' of the standard Lennard-Jones potential that is neglected during the simulation because of the use of a finite cut-off. For the atomistic models, such a contribution γ_{tail} was evaluated, after completion of the simulations, using the formula [36,57]

$$\gamma_{\text{tail}} = 12\pi\epsilon\sigma^6(\rho_L - \rho_V)^2 \times \int_0^1 \mathrm{d}s \int_{r_c}^{\infty} \mathrm{d}r \coth(rs/d)(3s^3 - s)r^{-3}, \quad (5)$$

with ϵ and σ as the Lennard-Jones parameters of the specific water model, ρ_L and ρ_V as the number densities of the liquid and vapour phases, r_c as the cut-off radius, and d as a thickness parameter. Specifically, d was obtained from the relation $t = 2.1972\,d$, where t is the '10–90 thickness', that is, the extent over which the interface density varies from $\rho_V + 0.1(\rho_L - \rho_V)$ to $\rho_V + 0.9(\rho_L - \rho_V)$. For the ELBA model, no tail correction needs to be considered, because the shifted-force Lennard-Jones potential (Equation (2)) is inherently zero beyond the cut-off.

2.4.2. *Electrical potential*

For an interface arranged parallel to the xy-plane, the electrical potential difference $\Delta\phi(z)$ from a reference point z_0 to a point z, defined as $\Delta\phi(z) := \phi(z) - \phi(z_0)$, can be calculated with [37]

$$\Delta\phi(z) = -\int_{z_0}^{z} E_z(z')\,\mathrm{d}z', \quad (6)$$

where E_z denotes the projection of the electric field on the z-axis (perpendicular to the interface). For atomistic models, where the electrostatics are typically represented with fixed point charges, $E_z(z)$ can be obtained as [37]

$$E_z(z) = \frac{1}{\varepsilon_0}\int_{z_0}^{z} \rho_q(z')\,\mathrm{d}z', \quad (7)$$

with $\rho_q(z')$ as the charge density. In our atomistic water simulations, the charge density was obtained with

$$\rho_q(z) = q_{\mathrm{O}}\rho_{\mathrm{O}}(z) + q_{\mathrm{H}}\rho_{\mathrm{H}}(z), \quad (8)$$

where q denotes the fixed (model-dependent) partial charge, $\rho(z)$ is the number density, and the subscripts O and H identify the oxygen and hydrogen atomic species [37]. For the ELBA water model, $E_z(z)$ is computed with [12,13,37]

$$E_z(z) = -\frac{\mu_z(z)}{\varepsilon_0}, \quad (9)$$

where $\mu_z(z)$ is the projection on the z-axis of the vector sum of the point dipole vectors.

A specific electrical property of interest for the liquid–vapour interface is the surface potential ϕ_{LV} (also called χ), which is the electrical potential difference between the liquid and the vapour phases [37,40,58].

To calculate the z-dependent electrical profiles from simulation, the relevant quantities were evaluated by summing and averaging over discrete slabs parallel to the xy-plane [12,13,37]; the thickness of each slab was 0.1 Å.

2.5. *Simulation timings*

To estimate the computational efficiency of ELBA, we conducted some comparative tests against SPC and TIP4P/2005; full technical details are reported in the supplementary material. In summary, ELBA proved to be between 40 and up to 100 times more computationally efficient than the atomistic models. While these figures are purely indicative and depend on many variables, they can be understood, at least in part, considering that the computational efficiency of an n-site water model is roughly proportional to $1/n^2$, as for every pair of interacting particles there are n^2 vectors to evaluate. Note, however, that the efficiency of ELBA is not only due to the model being single site, but also due to the enlarged timestep and the absence of long-range electrostatics (both typical features of coarse-grained approaches). It is relevant to note that the computational cost of long-range forces is especially high in large-scale parallel computing (due to communication overheads), and hence models that do not require them are expected to benefit the most from the ongoing and future increase in the number of processor cores characteristic of both conventional hardware architectures and graphics processing units [59,60].

3. Results and discussion

3.1. *Bulk liquid systems*

The density, potential energy, heat of vaporisation, and diffusion coefficient from the bulk water simulations are reported in Table 3, together with corresponding experimental data. The results obtained with ELBA are in overall good agreement with the experimental data, and in better agreement compared to some of the atomistic models. For density and diffusion, the high accuracy of ELBA is achieved through explicit fitting to experiment [12]. On the other hand, potential energy and heat of vaporisation were not targeted in the parametrisation; hence their good agreement with the experimental values is noteworthy. Atomistic

Table 3. Properties of bulk water at 298 K and 1 atm. Density: ρ. Potential energy: E_{pot}. Heat of vaporisation: ΔH_{vap}. Diffusion coefficient: D.

	ρ (g cm^{-3})	E_{pot} (kcal mol^{-1})	ΔH_{vap} (kcal mol^{-1} K^{-1})	D ($\times$ 10^{-9} m^2 s^{-1})
Experiment	0.997047[a]	−9.92[b]	10.52[c], 11.0[d]	2.3[e]
ELBA	0.99945(1)	−9.3145(1)	9.9068(1)	2.16(1)
SPC	0.97690(1)	−9.94832(7)	10.5404(1)	4.42(3)
SPC/E	0.99840(2)	−11.1562(1)	11.7484(1)	2.78(2)
TIP3P-Ew	0.99586(1)	−9.92777(8)	10.5199(1)	4.30(2)
TIP4P-Ew	0.99714(2)	−11.0877(2)	11.6798(2)	2.53(1)
TIP4P/2005	0.99846(4)	−11.4049(2)	11.9971(2)	2.28(2)

[a]Reference [61].
[b]Reference [62].
[c]Reference [63].
[d]Reference [4].
[e]Reference [64].

models are typically optimised to reproduce experimental density and heat of vaporisation, but not diffusion.

Oxygen–oxygen radial distribution functions are reported in Figure 1 (for ELBA, the oxygen position is mapped to the particle centre). The ELBA curve clearly deviates from the experimental and atomistic data; in particular, the two main peaks are shifted out by ≈0.4 Å and ≈1.5 Å, respectively. These results indicate that the local neighbourhood of an ELBA water particle is characterised by concentric shells of particles that are farther away with respect to the analogous shells in real (and atomistic) water. Detailed data of the height and location of the two main peaks for all models are tabulated in the supplementary material.

3.2. *Liquid–vapour interfacial systems*

3.2.1. *Structural features*

The structure of the liquid–vapour interface of water was investigated by computing mass density profiles along the direction (z) perpendicular to the interfacial plane (xy). From these profiles we obtained the densities ρ_L and ρ_V in the liquid and vapour phases, respectively, and the '10–90' thickness t, which is the extent over which the interface density varies from $\rho_V + 0.1(\rho_L - \rho_V)$ to $\rho_V + 0.9(\rho_L - \rho_V)$. The results of the calculation of these three structural properties for each model are reported in Table 4, together with corresponding experimental data. The full mass density curves as a function of z are reported in the supplementary material (Figures S6 and S7). Table 4 shows that the coarse-grained ELBA model reproduces the experimental liquid and vapour densities more closely than any atomistic model. While these seem impressive results for such a simple model, it should be clear that the specific (very high) level of agreement is fortuitous.

Regarding the '10-90 thickness' t, Table 4 shows that, for the atomistic models, t ranges from a minimum of 3.80 Å for TIP4P/2005 to a maximum of 4.70 Å for TIP3P-Ew; the ELBA value of 4.30 Å falls within this range. Unfortunately, these results cannot be clearly assessed, because the two available experimental data are very different from each other. In particular, while the simulation results broadly agree with the value of 4.1 Å from

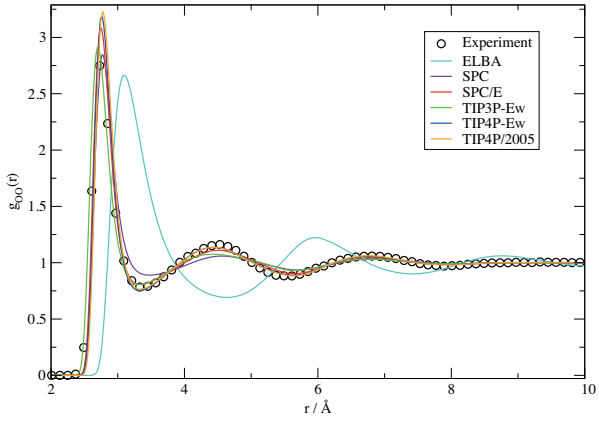

Figure 1. Oxygen–oxygen radial distribution functions. For clarity, some of the experimental data points are omitted; note, however, that the data point corresponding to the maximum height of the main peak has been preserved. The original full set of experimental data is available elsewhere [65].

Table 4. Structure of the liquid–vapour interface of water at 300 K. Density of the liquid phase: ρ_L. Density of the vapour phase: ρ_V. '10–90' thickness: t.

	ρ_L (g cm^{-3})	ρ_V (g cm^{-3})	t (Å)
Experiment	0.996515[a]	2.56×10^{-5}[b]	4.1[c], 8.3[d]
ELBA	0.99650(3)	2.6(2) $\times$ 10^{-5}	4.30
SPC	0.96439(2)	3.7(3) $\times$ 10^{-5}	4.60
SPC/E	0.98705(1)	8.7(4) $\times$ 10^{-6}	4.10
TIP3P-Ew	0.99301(1)	3.2(1) $\times$ 10^{-5}	4.70
TIP4P-Ew	0.98546(3)	4.2(3) $\times$ 10^{-6}	3.95
TIP4P/2005	0.99173(2)	4.7(9) $\times$ 10^{-6}	3.80

[a]Reference [61].
[b]Reference [66].
[c]Reference [67] from ellipsometric experiments.
[d]Reference [67] from X-ray reflectivity experiments.

Table 5. Surface tension of liquid–vapour interface at 300 K. For the atomistic models, the data format is $\gamma_P / \gamma_P + \gamma_{\text{tail}}$, where γ_P is the surface tension from Equation (4) and γ_{tail} is the tail correction (Equation (5)). Units are mN m^{-1}. Uncertainties in the simulation results are 0.1–0.2 mN m^{-1}.

Experiment	71.7[a]
ELBA	74.8
SPC	48.1/53.2
SPC/E	55.2/60.5
TIP3P-Ew	45.2/47.4
TIP4P-Ew	58.1/63.7
TIP4P/2005	64.6/68.4

[a]Reference [68].

ellipsometric experiments, they significantly differ from the value of 8.3 Å obtained from X-ray reflectivity experiments (both these experimental measurements were reported by Matsumoto and Kataoka [67]).

3.2.2. *Surface tension*

The surface tension values obtained from our simulations are reported in Table 5, together with the experimental measurement [68] at the same temperature (300 K). It can be seen that the ELBA model reproduces the experimental value more accurately than any atomistic model apart from TIP4P/2005, which shows a similar agreement (error of ≈3 mN m^{-1}) when the tail correction is included. Note that for ELBA no correction is required, because the shifted-force Lennard-Jones potential (Equation (2)) is natively zero beyond the cut-off distance, so there is no neglected tail to account for. It is important to stress that neither ELBA nor the atomistic models were parametrised to reproduce the surface tension, and hence this property is truly predicted. Given the simplicity of ELBA, its accuracy is especially remarkable.

3.2.3. *Vapour–liquid equilibria*

To further assess the ELBA model, we simulated the interfacial system at a range of increased temperatures (350, 400, 450, 500, 550 and 600 K). The resulting liquid–vapour phase diagram is plotted in Figure 2, together with experimental and atomistic simulation data from the literature. It can be seen that ELBA reproduces the experimental data more accurately than the popular TIP3P atomistic model, especially at high temperature. Compared to TIP4P/2005, which is arguably the most accurate atomistic model [43,69,70], the ELBA results are somewhat worse for the liquid phase, but they are slightly better for the vapour phase. The surface tension at different temperatures is plotted in Figure 3, again together with experimental and atomistic simulation data from the literature. The ELBA model reproduces the experimental behaviour very closely, at a level of accuracy comparable to that of TIP4P/2005

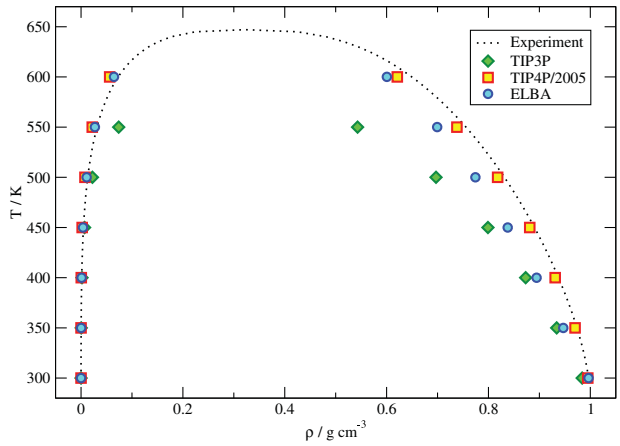

Figure 2. Vapour–liquid phase diagram. Experimental line from the NIST database [66]. Simulation data for TIP3P from Vega *et al.* [43], and for TIP4P/2005 from Alejandre and Chapela [71].

(and much higher than that of TIP3P). The surface tension data of ELBA were further processed to estimate the critical temperature T_c by fitting to the formula

$$\gamma = c_1(1 - T/T_c)^{11/9}\,[1 - c_2(1 - T/T_c)], \qquad (10)$$

which is commonly used to correlate surface tension data [41,43,71,72]. The best fit was achieved for $c_1 = 200.5$ mN m^{-1}, $c_2 = 0.3678$, and $T_c = 644.0$ K. This result for the critical temperature is in excellent agreement with the experimental value (647.1 K). For comparison, critical temperatures of 641.4 and 578 K have been reported for TIP4P/2005 [71] and TIP3P [43], respectively.

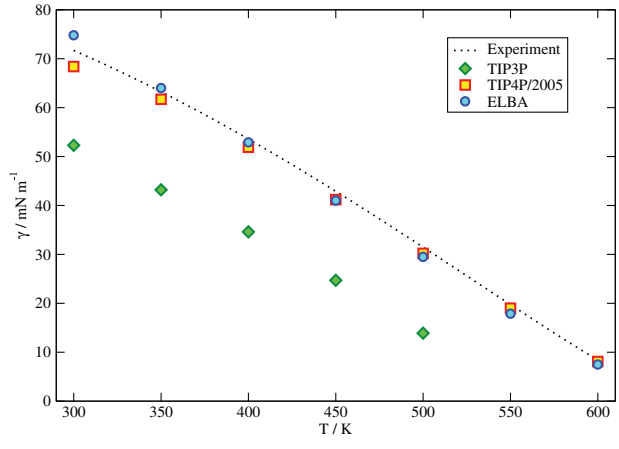

Figure 3. Surface tension at different temperatures. Experimental line from the NIST database [66]. Simulation data for TIP3P from Vega *et al.* [43], and for TIP4P/2005 from Alejandre and Chapela [71].

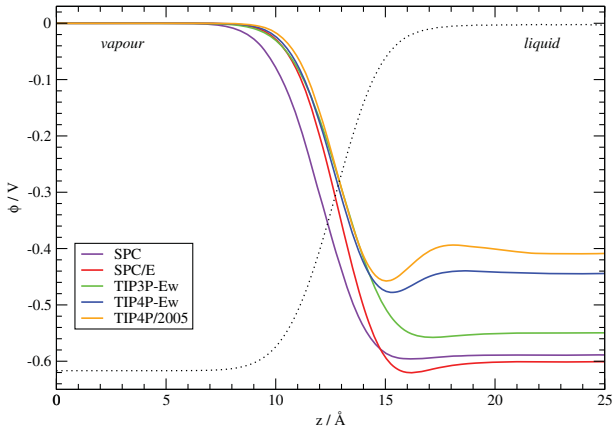

Figure 4. Electrostatic potential profiles. To assist interpretation, a representative mass density profile is also shown with a dotted line (the ordinate values of this profile are not on scale).

3.2.4. *Surface potential and electric field*

The electrostatic potential and electric field across the liquid–vapour interface were calculated from our simulations as detailed in Section 2.4.2. The profiles for the ELBA model were found to be constant and zero throughout. This absence of electrical features results from the lack of orientational ordering at the liquid–vapour interface, which is characteristic of spherical point dipole models [37,40,73]; since there is no preferential alignment of the dipoles, no electric field and potential difference arise. Before commenting on this behaviour, we shall analyse the electrical profiles of the atomistic models. It should be noted that while these properties have been previously published for SPC [74], SPC/E [37,40], and TIP4P-Ew [75], no previous calculation has been reported for the TIP3P-Ew model, and for the increasingly popular TIP4P/2005 model. The significant (non-constant) sections of the atomistic profiles are displayed in Figures 4 and 5 (the profiles across the entire length of the systems can be found in the supplementary material). It can be seen from Figure 4 that the potential changes very rapidly going from the vapour to the liquid phase; over a distance of only $\approx$5 Å, ϕ drops by $\approx 0.4 - 0.6$ V. In general, the spatial derivative of the potential gives (the negative of) the electric field; therefore, such a steep variation in ϕ is expected to correspond to very large field strengths. The depth-dependent electric fields are displayed in Figure 5; large peaks, in the range $\approx 1.3 - 1.6 \times 10^9$ V m^{-1}, can indeed be observed at $z = 12 - 13$ Å. In Figure 4, it can also be seen that after the steep drop all potential profiles reach local minima, and are then characterised by small increases, in proximity to the liquid phase, which are somewhat more pronounced for TIP4P-Ew and especially for TIP4P/2005. This behaviour is reflected in electric field troughs corresponding to the same region, as displayed in Figure 5 at $z = 16 - 17$ Å. While the troughs for SPC and TIP3P-Ew are almost negligible, the magnitude of the SPC/E trough reaches almost 1×10^8 V m^{-1}, while the troughs for TIP4P-Ew and TIP4P/2005 feature much larger magnitudes of 2.2×10^8 and 3.6×10^8 V m^{-1}, respectively.

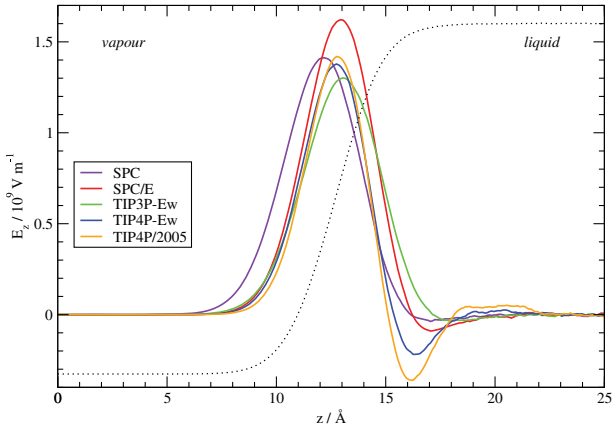

Figure 5. Projections of the electric field along the direction normal to the liquid–vapour interface (z-axis). To assist interpretation, a representative mass density profile is also shown with a dotted line (the ordinate values of this profile are not on scale).

Table 6. Surface potential of the liquid–vapour interface of water at 300 K.

Model	ϕ_{LV}/V
SPC	−0.5887(6)
SPC/E	−0.6006(7)
TIP3P-Ew	−0.5498(4)
TIP4P-Ew	−0.4443(5)
TIP4P/2005	−0.4080(7)

The numerical values of the surface potential ϕ_{LV} (the electrical potential difference between the liquid and vapour phases) are reported in Table 6. The values obtained range from ≈ -0.60 V for SPC/E to ≈ -0.41 V for TIP4P/2005. For ELBA, we observed a zero surface potential, as expected (see above). While this result, and the previously noted electrical profiles which are constant and zero through the interface, are certainly unrealistic, it is not straightforward to make a clear assessment. In fact, both the magnitude and sign of the true surface potential are disputed; while, as we have seen, standard atomistic models yield values around ≈ -0.5 V, the most recent experimental measurements range from $+0.025$ to $+0.24$ V [74,76], and density functional theory predicts $+3$ to $+4$ V [58,77–79].

4. Comparison between ELBA and other coarse-grained water models

Results obtained in this work for the ELBA model are compared in Table 7 with corresponding simulation data reported in the literature for alternative coarse-grained force fields. Considering single-site models like ELBA, relevant

Table 7. Properties of water in bulk and interface systems at 298/300 K.

	Mapping[a]	ρ (g cm^{-3})	E_{pot} (kcal mol^{-1})	D ($\times$ 10^{-9} m^2 s^{-1})	γ (mN m^{-1})
Experiment	–	0.997047[b]	−9.92[c]	2.3[d]	71.7[e]
ELBA	1 → 1	0.99945(1)	−9.3145(1)	2.16(1)	74.8(1)
SSD[f]	1 → 1	0.972–0.999	−9.60	1.78–2.51	–
SSDQO[g]	1 → 1	0.999[h]	–	2.21–2.26	–
M3B[i]	1 → 1	0.97(2)	–	1.7	–
mW[j]	1 → 1	1.001	–	6.5	66.0
MARTINI[k]	4 → 1	0.900[l]	–	2	30–45
P-MARTINI[m]	4 → 3	1.043	–	2.5	30.5
BMW[n]	4 → 3	1.047	–	–	77
GROMOS[o]	5 → 2	0.995	−5.569	6.9	51.2
WT4[p]	11 → 4	1.0001	–	2.23	17

[a]The notation $m \rightarrow n$ indicates that m water molecules are mapped to n interaction sites.
[b]Reference [61].
[c]Reference [62].
[d]Reference [64].
[e]Reference [68].
[f]References [80–82].
[g]References [90–92].
[h]Reference [92].
[i]Reference [95].
[j]Reference [96].
[k]Reference [97].
[l]Reference [99].
[m]Reference [98].
[n]Reference [99].
[o]Reference [101].
[p]Reference [103].

results have been reported in the literature for the SSD, SSDQO, M3B, and mW models. SSD is a model consisting of a Lennard-Jones sphere, a point dipole, and an additional octupolar term aimed at reproducing hydrogen bonding. SSD has been used to study liquid water and ice [80–83], and as a solvent in various systems [80,84–89]. In Table 7 we collect results obtained from various slightly different parametrisations of the SSD force field reported in the literature; good agreement with the experiment can be noticed in terms of bulk properties. Regarding the liquid–vapour interface, to our knowledge no results for SSD have been reported. SSDQO is a more elaborate version of SSD that includes quadrupolar and octupolar terms [90–92]. SSDQO has been used as a solvent for ions [93] and small molecules [94]. Like SSD, SSDQO reproduces accurately density and diffusion in the bulk; however, no simulations of liquid–vapour interfacial systems have been reported. M3B, which is unique in representing water–water interactions by a Morse potential, was developed as part of a coarse-grained force field for oligosaccharides [95]. M3B shows fairly good agreement with experiment in relation to density and diffusion. The mW model, which includes a three-body term to favour tetrahedral coordination, reproduces accurately density and surface tension; however, the diffusion coefficient is overestimated [96]. MARTINI is a popular model consisting of a Lennard-Jones potential without additional electrostatic terms, where each site maps four water molecules [97]. From Table 7, it can be seen that the bulk density of MARTINI is low compared to the other models, while the accuracy of the diffusion coefficient is comparable to that of most other models. In terms of interfacial properties, the surface tension of MARTINI is markedly lower than the experiment. P-MARTINI [98] refers to a polarisable version of MARTINI which consists of three sites, two of which are oppositely charged. This model improves substantially over the original MARTINI in terms of density, and its diffusion coefficient is also more accurate. However, the surface tension is less than half the experimental value. The BMW model [99] maps four water molecules to three charged sites and makes use of the Born–Mayer–Huggins potential instead of the Lennard-Jones potential. BMW has been applied to study the association between peptides in water [100]. The model reproduces well the experimental bulk water density and the surface tension. The GROMOS model [101] represents five water molecules with two oppositely charged sites. This model has also been used to solvate proteins [102]. The experimental density is reproduced accurately; however, potential energy and diffusion coefficient are somewhat less so. The value of the surface tension, while significantly lower than the experimental value, is better than several other coarse-grained models. WT4 is a model where groups of 11 water molecules are represented by 4 charged sites [103]. WT4 was employed to solvate ions and nucleic acids [103]. The

model reproduces well the experimental density and the diffusion coefficient; however, the surface tension is substantially smaller than the experimental value.

Overall, Table 7 shows that bulk liquid density and diffusion coefficient are reproduced accurately by most coarse-grained models. The density is typically used as a target in the parametrisation process; hence high accuracy should be expected. Regarding the calculation of the diffusion coefficient for those models mapping more than one real water molecule to a coarse-grained site, it should be noted that two different approaches are used. Some workers multiply the diffusion coefficient of the coarse-grained water by the number of real water molecules that a coarse-grained unit represents [97,98,103]; however, others do not apply such scaling [101]. Table 7 reports the diffusion data as originally published. The potential energy is reproduced fairly by ELBA and SSD and is overestimated by GROMOS, while to our knowledge it has not been reported for the other models. The experimental surface tension is reproduced rather well by ELBA, mW, and BMW, which in fact prove to be more accurate than most atomistic models (see Table 5), while the other coarse-grained models tend to underestimate this property to various degrees.

4.1. *Atomistic models: comparison between data from this work and from the literature*

In general, the results obtained here for the standard three- and four-site atomistic models are broadly consistent with available literature data for corresponding models and conditions [35,43,53,70,104–106]. In the following paragraphs, we consider specific comparisons with a focus on those cases where differences are not negligible.

Regarding SPC and SPC/E in the bulk, our results can be compared with those from Wu *et al.* [53]; while there is agreement for most properties, a small discrepancy can be noted for the diffusion coefficient, which we estimated to be 4.42 and 2.78, respectively, against the somewhat lower values 4.02 and 2.41 from Wu *et al.* [53] (all values in units of 10^{-9} m^2 s^{-1}).

Our results for the water–vapour interface at 300 K can be compared with the study by Ismail *et al.* [35], in particular regarding the surface tension (tail correction included). For TIP3P-Ew, we obtained the same result of 47.4 mN m^{-1}. However, for SPC/E, our value of 60.5 mN m^{-1} is larger than the value of 55.4 mN m^{-1} obtained by Ismail *et al.* [35]. For TIP4P-Ew, our result (63.7 mN m^{-1}) is also slightly larger than that (61.2 mN m^{-1}) of Ismail *et al.* [35]. It should be noted that the uncertainty in our results ($0.1 - 0.2$ mN m^{-1}) is significantly smaller than that ($2.4 - 3.0$ mN m^{-1}) reported by Ismail *et al.* [35].

Regarding TIP4P/2005, our results for bulk properties are consistent with those from Abascal and Vega [21]. As for the surface tension, our value of 68.4 mN m^{-1} is at the lower end of the range $68.4 - 69.5$ mN m^{-1} from the literature [41,42,71].

In terms of the surface potential, our values for SPC and SPC/E of -0.5887 V and -0.6006 V, respectively, are more negative than the often quoted literature data of -0.53 V [74] and -0.546 V [37], respectively, reported in the 1990s. However, our result for SPC/E is in excellent agreement with the value of -0.6003 V published recently by Horváth *et al.* [40]. For TIP4P-Ew, our calculation of -0.4443 V is somewhat less negative than the value of ≈ -0.52 V reported by Peng *et al.* [75]. Regarding both TIP3P-Ew and TIP4P/2005, to our knowledge the surface potential has not been previously reported.

Overall, our results for the atomistic water models are in good agreement with previous literature. A few small differences have been noted above for some models and some properties (mostly involving the liquid–vapour interface). One or more of the following factors are likely to be responsible for such discrepancies: system size, treatment of long-range interactions, treatment of short-range cut-offs, thermostat and barostat details, sampling and convergence issues, and details of the analysis of the raw data.

5. Conclusions

Bulk water and water–vapour systems were simulated to assess the coarse-grained ELBA model against results from common multi-site atomistic models and against literature data from experiments and other coarse-grained models. Many important properties were computed and compared, including density, potential energy, diffusion coefficient, and radial distribution function in the bulk, as well as structural, mechanical and electrical properties across the liquid–vapour interface. ELBA was shown to reproduce several experimental measurements as accurately as the best atomistic models, while being up to two orders of magnitude more computationally efficient. However, local spatial correlations in the bulk and electric features at the water–vapour interface were found to be missing. Work is underway to validate the use of ELBA as a solvent in multiscale dual-resolution simulations, where solutes (such as small molecules, peptides, and proteins) are represented with standard atomistic force fields.

Funding

This work was supported by the Engineering and Physical Sciences Research Council [grant code EP/G050708/1]. High-performance computational facilities were provided by the MidPlus regional centre of excellence [grant code EP/K000128/1].

Supplemental data

Supplemental data for this article can be accessed here.

References

[1] M. Chaplin, Nat. Rev. Mol. Cell Bio. **7**, 861 (2006).
[2] P. Ball, Chem. Rev. **108**, 74 (2008).
[3] T.A. Halgren and W. Damm, Curr. Opin. Struc. Biol. **11**, 236 (2001).
[4] B. Guillot, J. Mol. Liq. **101**, 219 (2002).
[5] K.A. Dill, T.M. Truskett, V. Vlachy, and B. Hribar-Lee, Annu. Rev. Bioph. Biom. **34**, 173 (2005).
[6] P. Paricaud, M. Predota, A.A. Chialvo, and P.T. Cummings, J. Chem. Phys. **122**, 244511 (2005).
[7] S. Mishra, N. Deeds, and G. Ruskauff, Ground Water **47**, 727 (2009).
[8] J.W. Ponder, C. Wu, P. Ren, V.S. Pande, J.D. Chodera, M.J. Schnieders, I. Haque, D.L. Mobley, D.S. Lambrecht, R.A. DiStasio, Jr., M. Head-Gordon, G.N.I. Clark, M.E. Johnson, and T. Head-Gordon, J. Phys. Chem. B **114**, 2549 (2010).
[9] X. He, W. Shinoda, R. DeVane, and M.L. Klein, Mol. Phys. **108**, 2007 (2010).
[10] C. Vega and J.L. Abascal, Phys. Chem. Chem. Phys. **13**, 19663 (2011).
[11] K.R. Hadley and C. McCabe, Mol. Simulat. **38**, 671 (2012).
[12] M. Orsi and J.W. Essex, PLoS ONE **6**, e28637 (2011).
[13] M. Orsi and J.W. Essex, Faraday Discuss. **161**, 249 (2013).
[14] G.S. Ayton, W.G. Noid, and G.A. Voth, Curr. Opin. Struc. Biol. **17**, 192 (2007).
[15] M. Orsi, W. Sanderson, and J.W. Essex, in *Molecular Interactions - Bringing Chemistry to Life*, edited by M.G. Hicks and C. Kettner (Beilstein-Institut, Frankfurt, 2007), pp. 85–205.
[16] S. Riniker, J.R. Allison, and W.F. van Gunsteren, Phys. Chem. Chem. Phys. **14**, 12423 (2012).
[17] H.J.C. Berendsen, J.P.M. Postma, W.F. van Gunsteren, and J. Hermans, in *Intermolecular Forces*, edited by B. Pullman (Reidel, Dordrecht, 1981), pp. 331–342.
[18] H.J.C. Berendsen, J.R. Grigera, and T.P. Straatsma, J. Phys. Chem. **91**, 6269 (1987).
[19] D.J. Price and C.L. Brooks III, J. Chem. Phys. **121**, 10096 (2004).
[20] H.W. Horn, W.C. Swope, J.W. Pitera, J.D. Madura, T.J. Dick, G.L. Hura, and T. Head-Gordon, J. Chem. Phys. **120**, 9665 (2004).
[21] J.L.F. Abascal and C. Vega, J. Chem. Phys. **123**, 234505 (2005).
[22] W.H. Stockmayer, J. Chem. Phys. **9**, 398 (1941).
[23] M. Neumann, Mol. Phys. **50**, 841 (1983).
[24] S.W. de Leeuw, J.W. Perram, and E.R. Smith, Annu. Rev. Phys. Chem. **37**, 245 (1986).
[25] J. Bartke and R. Hentschke, Phys. Rev. E **75**, 061503 (2007).
[26] L.E. Johnson, R. Barnes, T.W. Draxler, B.E. Eichinger, and B.H. Robinson, J. Phys. Chem. B **114**, 8431 (2010).
[27] J.D. Farrell, C. Lines, J.J. Shepherd, D. Chakrabarti, M.A. Miller, and D.J. Wales, Soft Matter **9**, 5407 (2013).
[28] A. Warshel, J. Phys. Chem. **83**, 1640 (1979).
[29] M.E. van Leeuwen, Fluid Phase Equilibr. **99**, 1 (1994).
[30] M.P. Allen and D.J. Tildesley, *Computer Simulation of Liquids*, 1st ed. (Oxford Science Publications, Oxford, 1987).
[31] D.C. Rapaport, *The Art of Molecular Dynamics Simulation*, 2nd ed. (Cambridge University Press, Cambridge, 2004).
[32] D.J. Adams, E.M. Adams, and G.J. Hills, Mol. Phys. **38**, 387 (1979).
[33] S.D. Stoddard and J. Ford, Phys. Rev. A **8**, 1504 (1973).
[34] S.L. Price, A.J. Stone, and M. Alderton, Mol. Phys. **52**, 987 (1984).
[35] A.E. Ismail, G.S. Grest, and M.J. Stevens, J. Chem. Phys. **125**, 014702 (2006).
[36] J. Alejandre, D.J. Tildesley, and G.A. Chapela, J. Chem. Phys. **102**, 4574 (1995).
[37] V.P. Sokhan and D.J. Tildesley, Mol. Phys. **92**, 625 (1997).
[38] Y. Fan, X. Chen, L. Yang, P.S. Cremer, and Y.Q. Gao, J. Phys. Chem. B **113**, 11672 (2009).
[39] G. Raabe and R.J. Sadus, J. Chem. Phys. **137**, 104512 (2012).
[40] L. Horváth, T. Beu, M. Manghi, and J. Palmeri, J. Chem. Phys. **138**, 154702 (2013).
[41] C. Vega and E. de Miguel, J. Chem. Phys. **126**, 154707 (2007).
[42] R.D. Mountain, J. Phys. Chem. B **113**, 482 (2009).
[43] C. Vega, J.L.F. Abascal, M.M. Conde, and J.L. Aragones, Faraday Discuss. **141**, 251 (2009).
[44] W.L. Jorgensen and J.D. Madura, Mol. Phys. **56**, 1381 (1985).
[45] R.W. Hockney and J.W. Eastwood, *Computer Simulation Using Particles*, 1sted. (Adam Hilger, New York, 1989).
[46] S. Plimpton, J. Comput. Phys. **117**, 1 (1995). http://lammps.sandia.gov.
[47] http://www.orsi.sems.qmul.ac.uk.
[48] T. Schneider and E. Stoll, Phys. Rev. B **17**, 1302 (1978).
[49] J.P. Ryckaert, G. Ciccotti, and H.J. Berendsen, J. Comput. Phys. **23**, 327 (1977).
[50] W. Shinoda, M. Shiga, and M. Mikami, Phys. Rev. B **69**, 134103 (2004).
[51] H.J.C. Berendsen, J.P.M. Postma, W.F. van Gunsteren, A. Di Nola, and J.R. Haak, J. Chem. Phys. **81**, 3684 (1984).
[52] D. van der Spoel, P.J. van Maaren, and H.J.C. Berendsen, J. Chem. Phys. **108**, 10220 (1998).
[53] Y. Wu, H.L. Tepper, and G.A. Voth, J. Chem. Phys. **124**, 024503 (2006).
[54] R.C. Tolman, J. Chem. Phys. **16**, 758 (1948).
[55] J.G. Kirkwood and F.P. Buff, J. Chem. Phys. **17**, 338 (1949).
[56] J. Janeček, J. Phys. Chem. B **110**, 6264 (2006).
[57] E. Blokhuis, D. Bedeaux, C. Holcomb, and J. Zollweg, Mol. Phys. **85**, 665 (1995).
[58] S.M. Kathmann, I.F.W. Kuo, C.J. Mundy, and G.K. Schenter, J. Phys. Chem. B **115**, 4369 (2011).
[59] T.D. Nguyen, J.M.Y. Carrillo, A.V. Dobrynin, and W.M. Brown, J. Chem. Theory Comput. **9**, 73 (2012).
[60] A. Shkurti, M. Orsi, E. Macii, E. Ficarra, and A. Acquaviva, J. Comput. Chem. **34**, 803 (2013).
[61] M. Tanaka, G. Girard, R. Davis, A. Peuto, and N. Bignell, Metrologia **38**, 301 (2001).
[62] D. Eisenberg and W. Kauzmann, *The Structure and Properties of Water* (Oxford University Press, Oxford, 1969).
[63] W. Wagner and A. Pruss, J. Phys. Chem. Ref. Data **31**, 387 (2002).
[64] M. Holz, S.R. Heil, and A. Sacco, Phys. Chem. Chem. Phys. **2**, 4740 (2000).
[65] A. Soper, Chem. Phys. **258**, 121 (2000). www.isis.stfc.ac.uk.
[66] E. Lemmon, M. McLinden, D. Friend, P. Linstrom, and W. Mallard, *NIST Chemistry WebBook* (National Institute of Standards and Technology, Washington, DC, 2011). http://webbook.nist.gov.
[67] M. Matsumoto and Y. Kataoka, J. Chem. Phys. **88**, 3233 (1988).
[68] N.B. Vargaftik, B.N. Volkov, and L.D. Voljak, J. Phys. Chem. Ref. Data **12**, 817 (1983).
[69] C. Vega, J.L.F. Abascal, and I. Nezbeda, J. Chem. Phys. **125**, 034503 (2006).

[70] H.S. Ashbaugh, N.J. Collett, H.W. Hatch, and J.A. Staton, J. Chem. Phys. **132**, 124504 (2010).
[71] J. Alejandre and G.A. Chapela, J. Chem. Phys. **132**, 014701 (2010).
[72] R. Sakamaki, A.K. Sum, T. Narumi, and K. Yasuoka, J. Chem. Phys. **134**, 124708 (2011).
[73] J.F.H. Stillinger and A. Ben-Naim, J. Chem. Phys. **47**, 4431 (1967).
[74] C.G. Barraclough, P.T. McTigue, and Y. Ng, J. Electroanal. Chem. **329**, 9 (1992).
[75] T. Peng, T.M. Chang, X. Sun, A.V. Nguyen, and L.X. Dang, J. Mol. Liq. **173**, 47 (2012).
[76] M. Paluch, Adv. Colloid Interfac. **84**, 27 (2000).
[77] S.M. Kathmann, I.F.W. Kuo, and C.J. Mundy, J. Am. Chem. Soc. **130**, 16556 (2008).
[78] S.M. Kathmann, I.F.W. Kuo, and C.J. Mundy, J. Am. Chem. Soc. **131**, 17522 (2009).
[79] K. Leung, J. Phys. Chem. Lett. **1**, 496 (2010).
[80] Y. Liu and T. Ichiye, J. Phys. Chem. **100**, 2723 (1996).
[81] A. Chandra and T. Ichiye, J. Chem. Phys. **111**, 2701 (1999).
[82] C.J. Fennell and J.D. Gezelter, J. Chem. Phys. **120**, 9175 (2004).
[83] C.J. Fennell and J.D. Gezelter, J. Chem. Theory Comput. **1**, 662 (2005).
[84] J. Michel, M. Orsi, and J.W. Essex, J. Phys. Chem. B **112**, 657 (2008).
[85] M. Orsi, D.Y. Haubertin, W.E. Sanderson, and J.W. Essex, J. Phys. Chem. B **112**, 802 (2008).
[86] M. Orsi, W.E. Sanderson, and J.W. Essex, J. Phys. Chem. B **113**, 12019 (2009).
[87] M. Orsi, J. Michel, and J.W. Essex, J. Phys.: Condens. Matter **22**, 155106 (2010).
[88] M. Orsi and J.W. Essex, Soft Matter **6**, 3797 (2010).
[89] M. Orsi, M.G. Noro, and J.W. Essex, J. R. Soc. Interface **8**, 826 (2011).
[90] T. Ichiye and M.L. Tan, J. Chem. Phys. **124**, 134504 (2006).
[91] S. Chowdhuri, M.L. Tan, and T. Ichiye, J. Chem. Phys. **125**, 144513 (2006).
[92] J.A. Te and T. Ichiye, J. Chem. Phys. **132**, 114511 (2010).
[93] M.L. Tan, L. Lucan, and T. Ichiye, J. Chem. Phys. **124**, 174505 (2006).
[94] J.A. Te, M.L. Tan, and T. Ichiye, Chem. Phys. Lett. **486**, 70 (2010).
[95] V. Molinero and W.A. Goddard, J. Phys. Chem. B **108**, 1414 (2004).
[96] V. Molinero and E.B. Moore, J. Phys. Chem. B **113**, 4008 (2009).
[97] S.J. Marrink, H.J. Risselada, S. Yefimov, D.P. Tieleman, and A.H. de Vries, J. Phys. Chem. B **111**, 7812 (2007).
[98] S.O. Yesylevskyy, L.V. Schäfer, D. Sengupta, and S.J. Marrink, PLoS Comput. Biol. **6**, e1000810 (2010).
[99] Z. Wu, Q. Cui, and A. Yethiraj, J. Phys. Chem. B **114**, 10524 (2010).
[100] Z. Wu, Q. Cui, and A. Yethiraj, J. Phys. Chem. Lett. **2**, 1794 (2011).
[101] S. Riniker and W.F. van Gunsteren, J. Chem. Phys. **134**, 084110 (2011).
[102] S. Riniker, A.P. Eichenberger, and W.F. van Gunsteren, Eur. Biophys. J. **41**, 647 (2012).
[103] L. Darré, M.R. Machado, P.D. Dans, F.E. Herrera, and S. Pantano, J. Chem. Theory Comput. **6**, 3793 (2010).
[104] L.X. Dang and T.M. Chang, J. Chem. Phys. **106**, 8149 (1997).
[105] A. Glättli, X. Daura, and W.F. van Gunsteren, J. Chem. Phys. **116**, 9811 (2002).
[106] S. Tazi, A. Boţan, M. Salanne, V. Marry, P. Turq, and B. Rotenberg, J. Phys.: Condens. Matter **24**, 284117 (2012).